UC Irvine
UC Irvine Electronic Theses and Dissertations

Title

Optimization of a Deep Learning Framework Used for Phase-Change Analysis

Permalink

https://escholarship.org/uc/item/16p9q910

Author

Simadiris, Peter

Publication Date

2021

Copyright Information

Peer reviewed|Thesis/dissertation

UNIVERSITY OF CALIFORNIA,
IRVINE

Optimization of a Deep Learning Framework Used for Phase-Change Analysis

THESIS

submitted in partial satisfaction of the requirements
for the degree of

MASTER OF SCIENCE

in Mechanical and Aerospace Engineering

by

Peter Simadiris

Thesis Committee:
Assistant Professor Yoonjin Won, Chair
Assistant Professor Ramin Bostanabad
Assistant Professor Aparna Chandramowlishwaran

2021

TABLE OF CONTENTS

LIST OF FIGURES

ACKNOWLEDGMENTS

ABSTRACT OF THE THESIS

Optimization of a Deep Learning Framework Used for Phase-Change Analysis

By

Peter Simadiris

Master of Science in Mechanical and Aerospace Engineering

University of California, Irvine, 2021

Assistant Professor Yoonjin Won, Chair

The continuous increase in the performance of high-power energy systems calls for thermal management systems capable of dissipating large concentrations of heat. Phase change cooling strategies utilize latent evaporation energy to absorb substantial amounts of heat. Although phase change cooling has considerable potential in thermal management, little research has been done regarding the optimization of these systems. The extreme volatility within phase change processes poses a challenge for researchers to obtain measurements with any reasonable uncertainty. Essential to altering the heat transfer performance is understanding nucleation dynamics, which involves quantifying individual nucleation features as well as their correlation to system properties. The complex dynamics within these systems prevent accurate extraction of nucleation statistics using conventional methods. Recent progression in machine learning enables researchers to automatically quantify these system dynamics. For instance, a 10 second dataset composed of high-speed boiling images normally contains at least one million bubble features, where an experiment will likely exceed millions of bubble features. To accurately extract data from these systems requires an extensive amount of time as well as an in depth understanding of the underlying physics. Inspired by this challenge, this thesis reports an autonomous vision-based framework capable of measuring nucleation dynamics at a high-temporal, microscopic scale.

We employ a modular framework that consists of an artificial intelligence (AI) based object detection and object tracking to study nucleation dynamics occurring within phase change systems including pool boiling, dropwise condensation, and film wise condensation. Vital nucleation statistics are extracted by tracking individual droplets within phase change systems using sequential high-speed, high-resolution images.

CHAPTER 1

Introduction

Chapter 1 introduces how phase change processes can fulfill the growing need for high heat-flux thermal management systems. Various methods used in past studies to analyze phase change systems are discussed as well as how recent advancements in machine learning enable researchers to study highly complex systems at extreme resolutions.

1.1 Thermal Management

Thermal management systems currently limit the performance of high-power electronic devices such as laser diodes, nuclear reactors, microprocessors, and heat exchangers due to the inability to dissipate substantial amounts of heat. [1-3] Recent declines in transistor density illustrate the dependency between microprocessors and thermal management. On the microscale, modern microprocessor designs report a heat generation up to $400\ W/cm^2$.[4] For example, approximately 30-55% of the total energy used by data centers is allocated to thermal management.[5] This intense heat generation reduces microprocessor lifetime, performance, and durability. Thus, thermal engineers seek effective high heat flux thermal management systems.

Commonly, high heat flux thermal management systems implement phase change cooling setups due to the ability to absorb ample heat loads. Phase change cooling utilizes the latent evaporation energy of the working fluid during liquid-to-vapor phase change to dissipate large amounts of heat within a small temperature gradient. Current phase change cooling systems include condensation [6], pool boiling [7], flow boiling [8], jet impingement [9], microchannel heat sinks [10], and spray cooling.[11] Among numerous approaches to improve

phase change heat transfer performance, processes governed by nucleation dynamics such as pool boiling, flow boiling, and dropwise condensation have gained interest due to recent advancements in measurement techniques, in particular artificial intelligence.
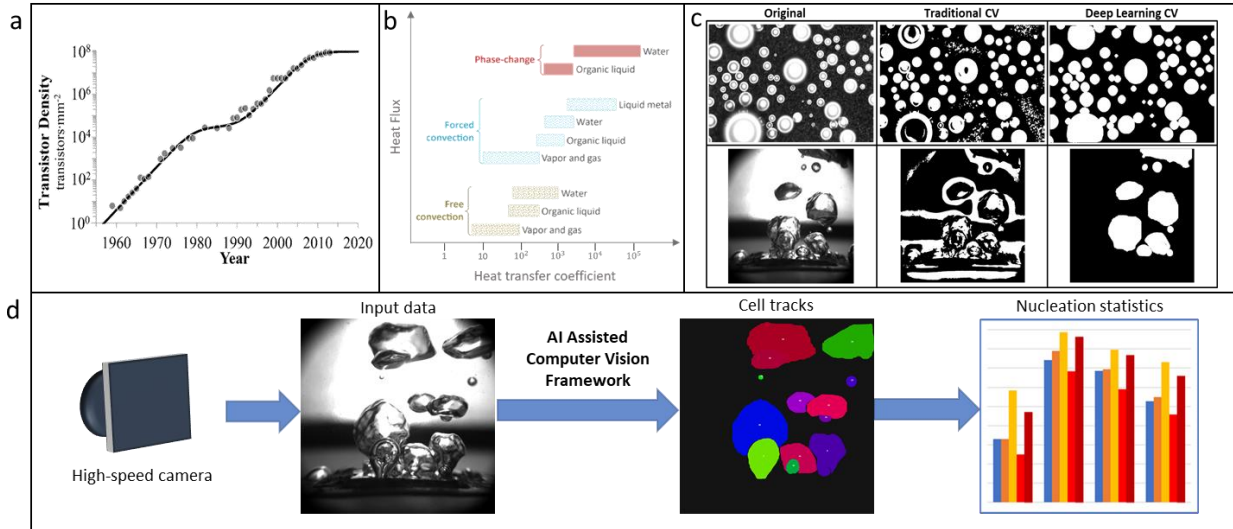
Figure 1. Microprocessor evolution over seven decades (a). Heat transfer coefficient for various thermal management processes and working fluids (b). The prediction capability of the framework is compared to conventional computer vision techniques (adaptive thresholding) (c). An overview of the computer vision framework. (d)

1.2 Previous Studies about Phase Change Analysis

Over the past decades, extracting nucleation statistics within phase change processes has been a challenging task for thermal engineers. Quantification of nucleation statistics has been widely investigated using numerical, theoretical, and experimental methods. Past heat transfer models utilize theoretical-empirical correlations to mitigate the complex physical mechanisms governing these nucleation dynamics.[12-14] For example, past theoretical studies simplified heat transfer models by excluding mid-to-high heat flux regimes near CHF.[15] Studies also assumed perfect spherical shape for bubbles to reduce model complexity.[16] Previous literature also studied the effect of nucleation dynamics using

2

numerical and experimental methods. However, due to the complexity within phase change systems, results documented from direct numerical simulations of phase change processes are debatable.[17] This compels researchers to mostly rely on experimental methods to measure heat transfer performance (thermocouples, multimeters).

Past studies also utilized infrared thermography to measure the distribution of liquid and gas phases in contact with the heater surface. The studies found that the wetted area fraction decreases with increasing heat flux.[18] Jiangliang et. al employed a charge-coupled device (CCD) camera to record bubble behavior and found that transient conduction due to bubble interactions is the main mechanism resulting in high heat transfer rates during coalescence.[19] Lee et. al utilized thermometers, multimeters, and heater surface area to quantify the effect of ultrasonic actuation on nucleation dynamics. This study reported a 17% increase in the heat transfer coefficient when ultrasonic actuation is used within the nucleate boiling regime.[20] Barbosa et. al utilized high-speed video recordings to quantify and predict annular flow dynamics.[21] Waltrich et. al used high-speed video recordings to produce transitional models for slug, churn, and annular flow. It was reported that churn flow is present where previous studies regarded the flow regime as underdeveloped slug flow.[22] Consequently, phase change heat transfer models vary depending on the assumptions specified or lack high heat flux regime information altogether.

1.3 Introduction to Convolutional Neural Networks

A favorable approach to tackling the daunting challenge of quantifying nucleation dynamics is to use an instance segmentation-based framework to identify and track bubbles within phase change systems. For decades, image classification tasks have been performed using classic computer vision (CV) methods such as thresholding, clustering, region growing, and

edge detection.[23] These techniques require an extensive understanding to create detectable features associated with objects of interest. Global thresholding is a CV technique that selects a threshold value as the cutoff value for binary classification. However, binary classification automatically prohibits individual droplet tracking, ruling out analysis of bubble density, count, distribution, etc. A major downside to traditional CV methods is that handwritten detection features are susceptible to incorrect detections due to data variance. For example, if light reflects over the region of interest, the object will not appear as expected and will not be correctly detected. Adaptive thresholding is a CV technique that adjusts the threshold value within the image to account for data variance. However, Figure 1c shows that neither threshold can successfully detect complex bubble morphology within phase change processes. This vulnerability to data variance is a critical demise of traditional computer vision techniques.

However, rapid progression in computer vision methods employing convolutional neural networks (CNNs) have enabled researchers to develop frameworks to autonomously extract nucleation dynamics using high-speed image datasets. CNN models achieve improved performance compared to conventional CV methods due to their ability to efficiently learn and recognize features within images similarly to the human brain's visual system.[23] Recently, the majority of AI based computer vision frameworks utilize CNNs to track various objects. CNN models are currently solving challenging image classification tasks in various fields such as autonomous driving [24], wildlife monitoring [25], and agricultural surveying.[26] CNNs are used to extract distinct hierarchical features within images to track and study objects.[27] Rudimentary features such as curves and edges are at the lowest level of the hierarchy, while the IDs of bubbles are at higher levels. These features are later sent

4

through a state-of-the-art tracking module to determine the bubble location, size, eccentricity, and other bubble characteristics.

Recently, thermal engineers recognized the capability of CNNs to measure slight variations between images to extract nucleation statistics. Hobold et. al detected and classified pool boiling regimes using a custom machine learning vision-based framework.[28] Another report introduces real-time heat flux quantification utilizing visualization-based data and a neural network-based model with errors as low as 7%.[29] A recent study presents a CNN-based instance segmentation framework to study dropwise condensation heat transfer at a microscopic scale (300nm) with a 200ms time resolution.[30]

1.4 Scope of Thesis

The objective of this thesis is to present a novel AI assisted vision-based framework capable of accurately quantifying complex nucleation dynamics occurring within phase change experiments. Training and optimization of the framework is thoroughly explained in the Methods section so that thermal engineers could setup, optimize, and integrate the framework into their laboratory.

CHAPTER 2

Methodology

Chapter 2 introduces the metrology that is used to extract bubble features within phase change systems. Mask R-CNN model training is discussed as well as an overview of the experimental setups used to record the phase change processes.

2.1 Deep Learning CV Framework

2.1.1 Framework Summary

To study nucleation dynamics occurring within phase change systems, we developed a CNN based framework composed of an object detector and a tracking module to identify and track individual droplets within sequential high-speed, high-resolution images. The objector detector utilizes a deep learning instance segmentation model, MASK R-CNN to identify and assign unique IDs to individual droplets. The detector generates a grey-scale pixel wise mask containing spatial features, such as bubble size and location. Sequential images containing unique IDs and spatial information are then processed in the tracking module (TrackPy) where k-dimensional (k-d) tree algorithms track spatial features for each time step and compute the most probable trajectory for each ID. Potential errors in individual trajectories can be manually verified and mitigated using a graphical user interface (GUI) derived from PyQt and PyQtGraph libraries.[31] The spatiotemporal features for individual bubbles are recorded in a spreadsheet file where algorithms containing derived energy balance equations can be implemented to quantify high-level system properties to study nucleation dynamics and heat transfer properties.

This high-resolution spatiotemporal data enables heat transfer models to account for complex coalescence events for the first time. Bubble features (i.e., location, size) can identify

departure events, calculate void fraction, compute individual droplet growth rate, detect surface deterioration, and recognize onset of critical heat flux. The same bubble features are used to calculate bubble density, rising velocity, and size distribution. Departure physics is particularly important in nucleate boiling experiments, where departure characteristics (i.e., velocity, frequency) exhibit a large impact on heat transfer performance. Void fraction information within flow boiling systems can determine the onset of critical heat flux within flow boiling systems. Individual droplet heat transfer rate is essential to understanding the relationship between droplet growth rate and size distribution. These bubble statistics are required to quantify high level system properties such as heat transfer rate per bubble and bubble density.[32] These high-level properties are used to calculate total surface heat flux, which defines overall heat transfer performance.

2.1.2 Mask R-CNN Model Training

MASK R-CNN is a CNN that extracts features from images which can be used to quantify system dynamics. MASK R-CNN is an instance segmentation model that outperforms most state-of-the-art methods.[23] The images generated from MASK R-CNN are used to obtain spatiotemporal data from each object. MASK R-CNN is a supervised learning model, which requires a labeled training dataset to learn the features of an object.[23] A durable, pretrained CNN model, VGG16, was chosen for this framework.[33] Although the model is pretrained, the feature weights must be adjusted for the desired object of interest (e.g., bubbles). The training dataset was annotated using an online commercial software (Supervisely, San Jose, CA, USA) where the regions of interest were highlighted, as shown in Figure 3. To mitigate possible bias, the training dataset consisted of randomized images. Phase change experts carefully labeled each bubble to ensure that the model accurately learns to detect bubbles. Depending on the complexity of the system, this could take

thousands of images. The annotation process was reduced to 50 images by utilizing data augmentation techniques, which help improve the generalizability of the model by inputting slightly modified versions of the training dataset. The augmented training dataset contains 704 images where 80% are used for training, and 20% are used to test the model. The pretrained model begins with weights from the Microsoft Common Objects in Context (MSCOCO) dataset.[34] These feature weights are adjusted during training to detect the object of interest. The model trains for 100 epochs with a stochastic gradient descent using a learning rate of 1e-3 and a momentum of 0.9. After each epoch, the weights are adjusted to minimize error. The results in Figure 2 show that the training and test loss both decrease, with a minimum test less of 0.09 at epoch 98. The model with the lowest losses is selected for this study. Figure 3 displays an overview of training an AI assisted vision-based framework using a custom training dataset.
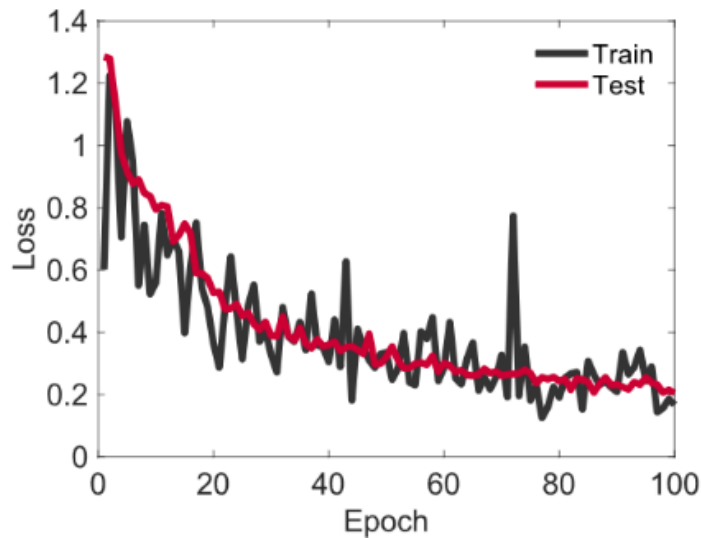
Figure 2. Training and testing losses shown during CNN model training. Losses continue to decrease as the model adjusts the feature weights for more accurate predictions.[30]
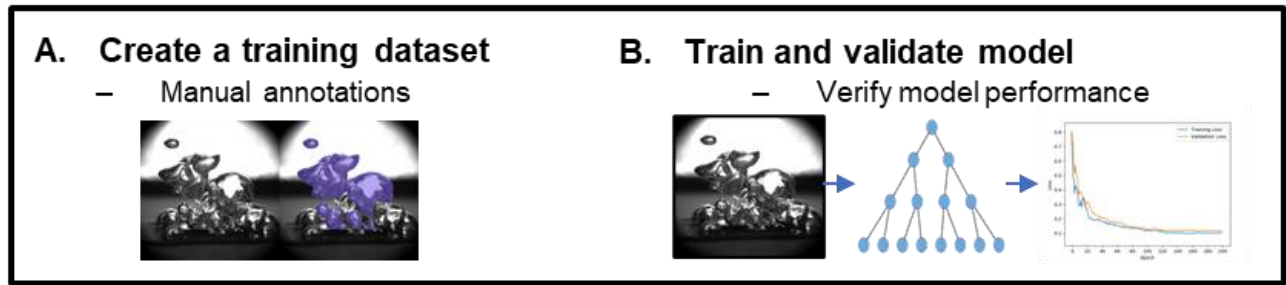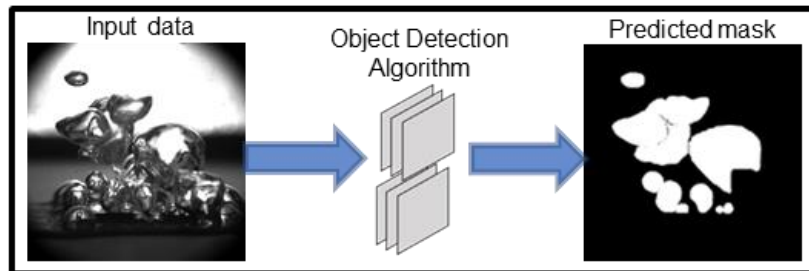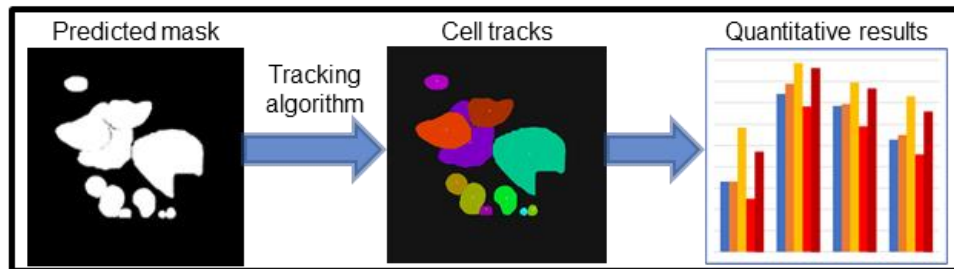
Figure 3. An overview of the steps to extract nucleation statistics using artificial intelligence and a custom training dataset.

2.2 Data Acquisition

2.2.1 Boiling Setup

High resolution images were captured from four consecutive pool boiling experiments conducted in the UCI Won Lab. The pool boiling apparatus composed of a guard heater, boiling chamber, boiling surface, heating block, four cartridge heaters, thermocouples connected to a data acquisition device, and a high-speed camera. The boiling surface consisted of a 1 cm x 1 cm copper square soldered to the heating block. Thermal paste was evenly coated

on the sample to ensure accurate thermocouple measurements. The boiling chamber and surface were both thoroughly cleansed using a piranha solution for five minutes before each experiment. The heating block used four cylindrical cartridge heaters powered by an AV voltage regulator (Variac Transformer) within a copper block wrapped in fiberglass insulation to promote thermal equilibrium. The guard heater connected to a PID controller maintained saturation conditions within the degassed, deionized water. Heat flux is calculated using $q'' = k\Delta T/L$, where ΔT is the temperature difference from equally spaced thermocouples at a distance L. The uncertainty within the thermocouple measurements is ± 1 °C. Thermal stability within the temperature readings must be observed before any data collection can occur to ensure consistent results. The data acquisition device (LabJack U6) measures and records the thermocouple readings throughout the experiment. A high-powered LED light paired with a light diffuser were placed behind the boiling chamber to promote illumination. The images are captured with a high-speed camera (DS-Qi2, Nikon) mounted on a fixture. Images are captured with a resolution of 1024 x 1024 pixels for approximately 3 minutes for each heat flux step. A high resolution was selected to ensure sufficient bubble statistics were captured. High speed capture rates of 2,000 fps further improve image quality by minimizing motion blur. However, a disadvantage to using a high capture rate is the increased probability of potential bias when training the model with highly similar images. To mitigate any bias and increase model generalizability, randomized images were captured for a 30 second period to be used for training.
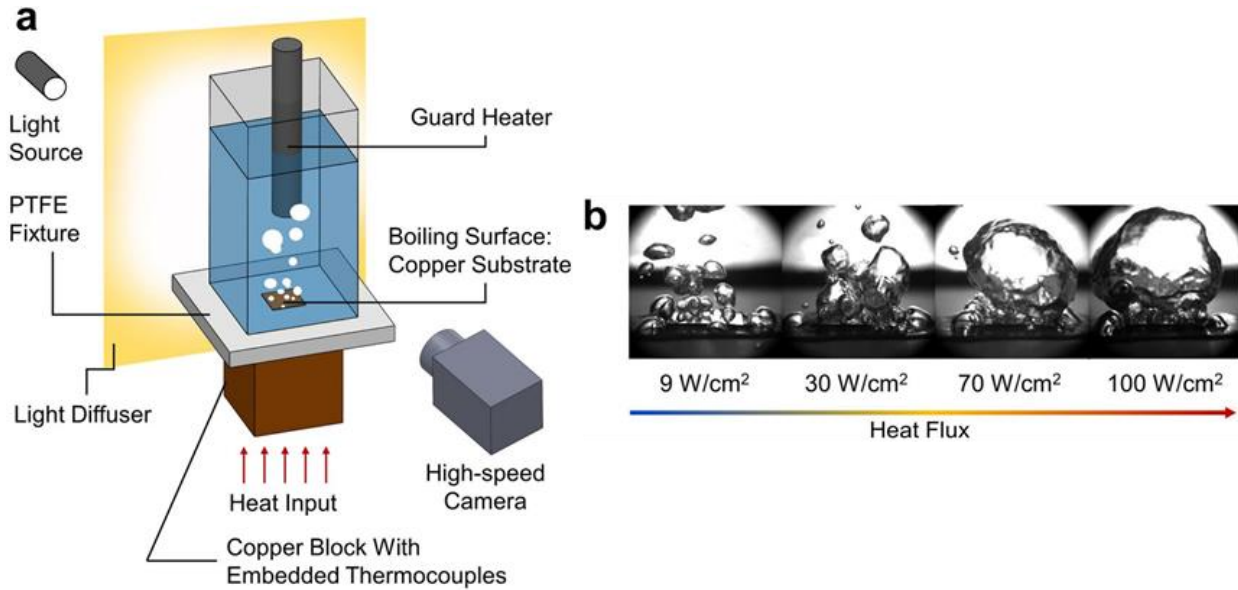
Figure 4. Schematic of pool boiling experimental setup (a). Boiling images captured from the experimental setup verify the complexity of bubble growth as heat flux increases (b). [35]

2.2.2 Condensation Setup

The condensation dataset was obtained from a custom-made droplet coalescence optical light microscopy setup. Silicon wafers were thoroughly cleaned using acetone and isopropyl alcohol, rinsed with distilled water, and dried with nitrogen. Silicon wafers were cut into 2 cm x 2 cm squares and coated with 100 nm thickness of octafluorocyclobutane (C_4F_8) to exhibit hydrophobic properties. The wafers were horizontally mounted onto a cold stage (Instec, TP104SC-mK2000A) utilizing thermal grease (Omegatherm, Omega, thermal conductivity of 2.2 W/m·K) and maintained at the test temperature of $T_w = \pm 1$ °C in a laboratory temperature of $T_{air} = 22 \pm 0.5$ °C with a relative humidity of $\Phi = 28 \pm 1\%$ (Roscid Technologies, RO120). (EnDrJm) The condensation dataset was captured at a resolution of 800 x 600 pixels using a high-speed camera (Eclipse LV100, Nikon) mounted to an upright microscope (Phantom, V711, Vision Research). An LED light was utilized to increase illumination to obtain clear images.
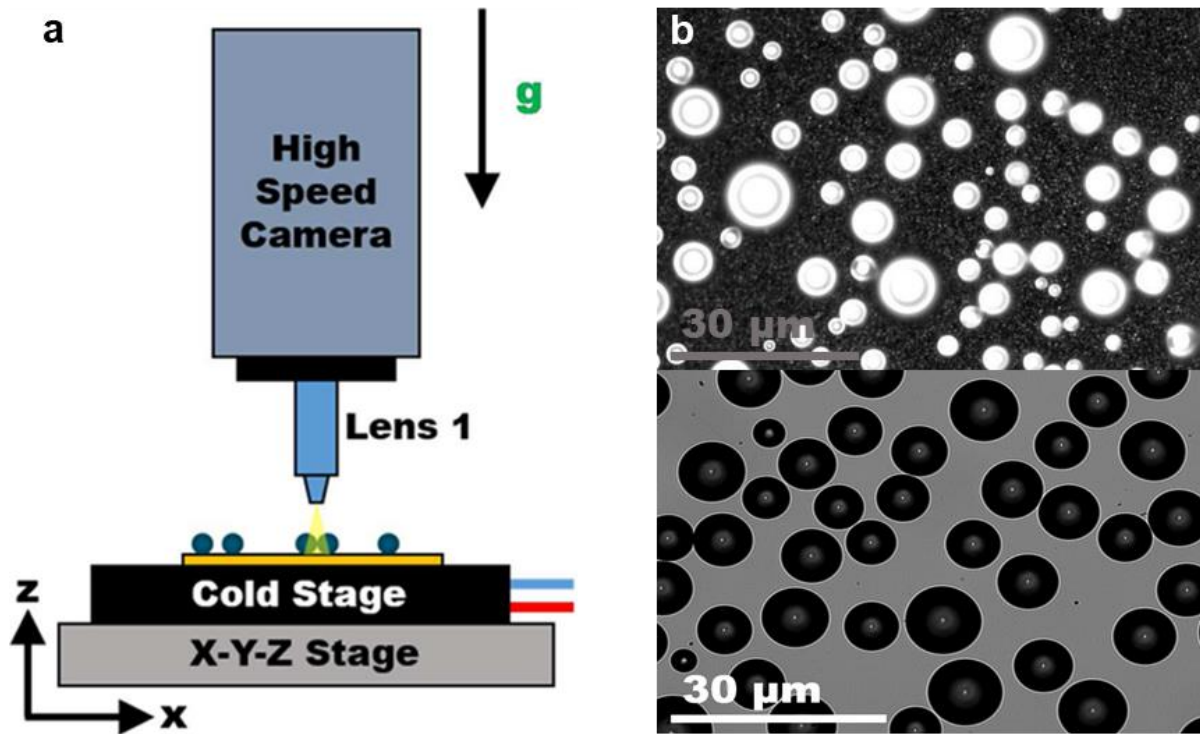
Figure 5. Schematic of dropwise condensation experimental setup shown in (a). Top-view condensation images captured at extreme spatiotemporal resolution of 300 nm and 200 ms (b).[36]

2.2.3 Data Augmentation

Data augmentation strategies are used to maximize the generalizability of the training images by generating a large dataset consisting of slight alterations of an original dataset.[37] The images were flipped along the vertical and horizontal axis, as well as rotation and size adjustment. Other augmentation techniques included adjusting image brightness, introducing gaussian noise, and cropping. 704 augmented images are generated from 50 original images. These techniques directly reduce the amount of annotated data required; a laborious, time-consuming task required to train the model.
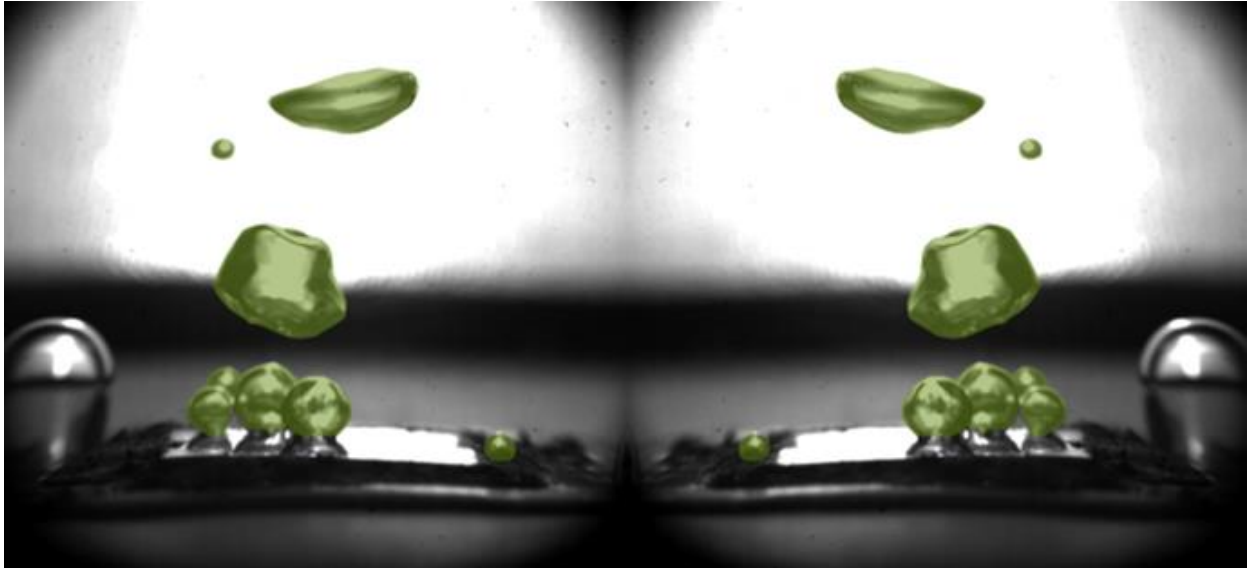
Figure 6. Data augmentation performed on a pool boiling image. The image presents a rotation augmentation along the vertical axis.

CHAPTER 3

Results and Discussion

Chapter 3 reviews the performance of the model with respect to runtime, image size, and heat flux. The prediction performance metrics used to evaluate the model are discussed as well as different types of errors that vision-based frameworks encounter when tracking nucleation dynamics. The methodology developed to optimize model predictions is also discussed.

3.1 Runtime and Accuracy Tradeoff

The tradeoff between runtime and precision becomes particularly important for real-time frameworks. A high-resolution image will require an increase in runtime but contains more information (pixels) than a low-resolution image. This results in a more precise prediction at the cost of runtime. Figure 7 shows the runtime for various image resolutions and the corresponding precision values for our framework. The figure shows that as image resolution increases, runtime and precision increase together. The increase in performance is due to higher resolution images containing more pixels. The large spike in runtime is due to the model training dataset image resolution being 1024 x 1024. It must be noted that high-

resolution images are vital for detecting smaller objects (i.e., condensation droplets), but not as critical for larger objects (i.e., high heat flux coalescence).
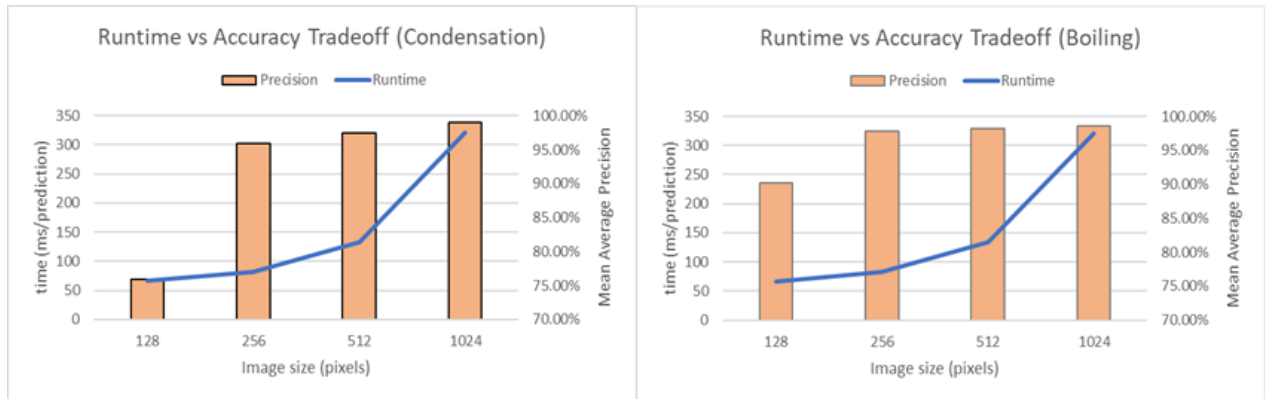
Figure 7. The tradeoff between runtime and precision is shown for boiling and condensation datasets.

3.2 Mask R-CNN Prediction Performance

A script is developed to determine the performance of the model using a commercial programming software (MATLAB). The script binarizes the predicted dataset and ground truth dataset, then checks if the predicted dataset pixels correspond with the ground truth pixels. A true condition occurs when pixels are equal to each other, similarly a false condition occurs when the pixels do not equal each other. A positive condition is when the model detects an instance, whether it is true or false. A negative condition is when the model does not detect an object.[38] That is, true and false positive (TP/FP) is defined as the number of positives that were correct/incorrect and is similarly defined for true and false negatives (TN/FN). These conditions are summed across the dataset and used to determine the performance of the model. An overview of the image adjustments is shown below.
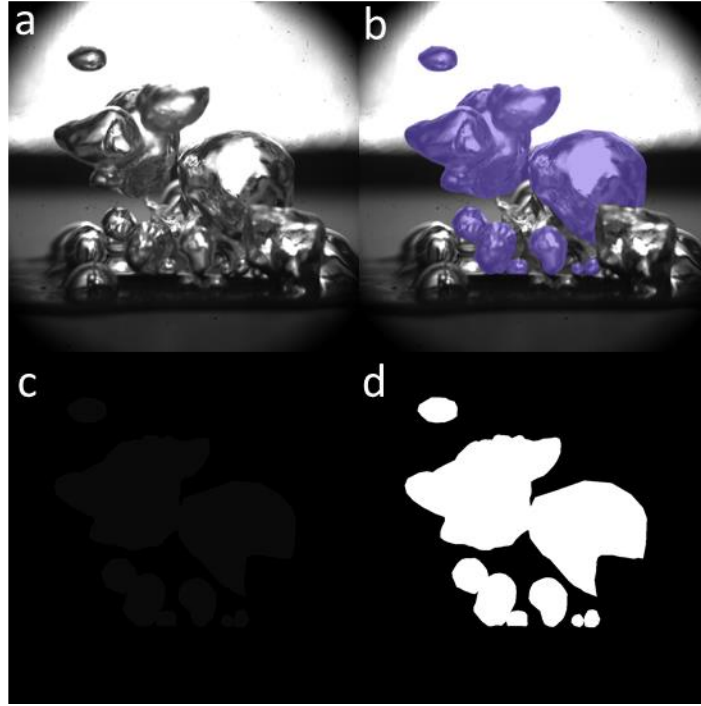
Figure 8. Pool boiling image captured via high-speed camera (a). Annotated ground truth segmentation mask (b). Mask-RCNN greyscale mask detection (c). Mask-RCNN binary mask used for performance analysis (d).

The performance metrics used to validate the model were accuracy, recall, precision, and F1 score, and mean average pixel error (MAPE). Accuracy is the ratio of the sum of true positive instances to the overall positive instances, showing how often the model predicts a pixel correctly.[39]

$$Accuracy = \frac{True\ Positives + True\ Negatives}{True\ Positives + True\ Negatives + False\ Negatives + \ False\ Positives}$$

Recall is the ratio of true positive instances to the sum of overall true positive instances and false negative instances, representing how often the model predicts a true positive instance correctly with respect to all observed positive instances.[39]

$$Recall = \frac{True\ Positives}{True\ Positives + False\ Negatives}$$

Precision is the ratio of true positive instances to the sum of all observed true instances. This describes how often a positive instance was correctly predicted compared to all positive instances.[39]

$$Precision = \frac{True\ Positives}{True\ Positives + False\ Positives}$$

F1 score is the weighted average of recall and precision and does not include true negative instances. It can be used as an alternative to accuracy when true negatives are not considered significant observations.[39]

$$F1\ Score = 2 * \frac{(Precision * Recall)}{(Precision + Recall)}$$

MAPE was determined by subtracting the ground truth binary mask from the predicted binary mask, then dividing by the ground truth. An example of the subtracted mask is shown below.

Figure 9. Subtracted binary mask where white pixels indicate a false negative detection.
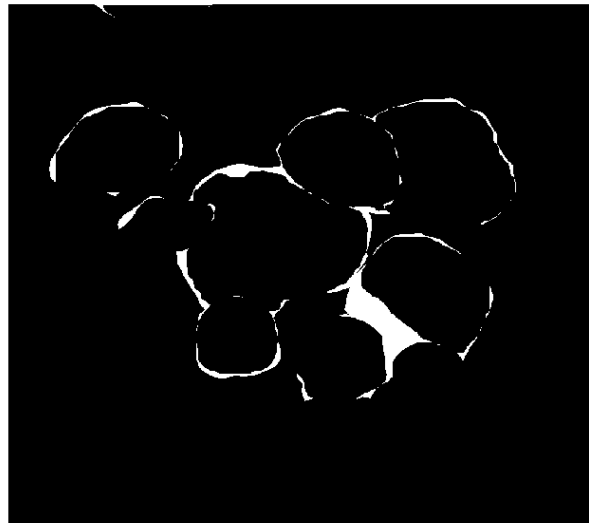
This results in the true negatives being removed from the binary matrix, leaving only true positives, false positives, and false negatives. Similar to recall, MAPE compares the ratio of predicted positive pixels to overall positive pixels.

17

$$imageData = \frac{(groundTruth - prediction)}{(groundTruth)} \qquad MAPE = \frac{True\ Positives}{True\ Positives + False\ Negatives}$$

Our framework displays striking performance (>94%) based on multiple object detection performance metrics including precision, recall, F1 score, MAPE, and occlusion-induced pixel error (OPE). The maximum error can be seen in Figure 10, denoted by the largest MAPE. Prediction performance overall declines as heat flux increases due to the increase in bubble-to-bubble interactions occurring near the boiling surface. The growth in coalescence events leads to nucleating bubbles being partially or fully covered, resulting in an inaccurate detection (occlusion). Condensation and low heat flux datasets have superior results compared to mid-to-high heat flux datasets due to occlusion-based events. Film-wise condensation achieves outstanding performance compared to pool boiling because condensation is a less volatile phase change process. At 30W, few bubbles form at the surface and there are minimal coalescence events. Model performance decreases from 30W to 50W due to the increase in coalescence events covering bubbles. However, model performance starts to increase around 90W once coalescence events begin to decrease and bubbles begin to merge into large, singular clusters. Figure 13 shows how occlusion-based events increase as a function of heat flux.

3.3 Mask R-CNN Compared to Traditional Computer Vision Methods

To compare traditional computer vision methods with our model, global and adaptive thresholding methods were tested using MATLAB Image Segmentation Functions, *graytresh* and *adaptthresh*. The prediction performance for each segmentation method is shown Figure 11. Although global thresholding achieves comparable performance to Mask R-CNN, MATLAB image segmentation functions do not provide instance-wise segmentation masks nor are the results accurate enough to track nucleation events. This is a major downfall because the segmented masks cannot be used to track nucleation events without instance-

wise information. However, Mask R-CNN is the only autonomous segmentation method capable of extracting instance-wise data.
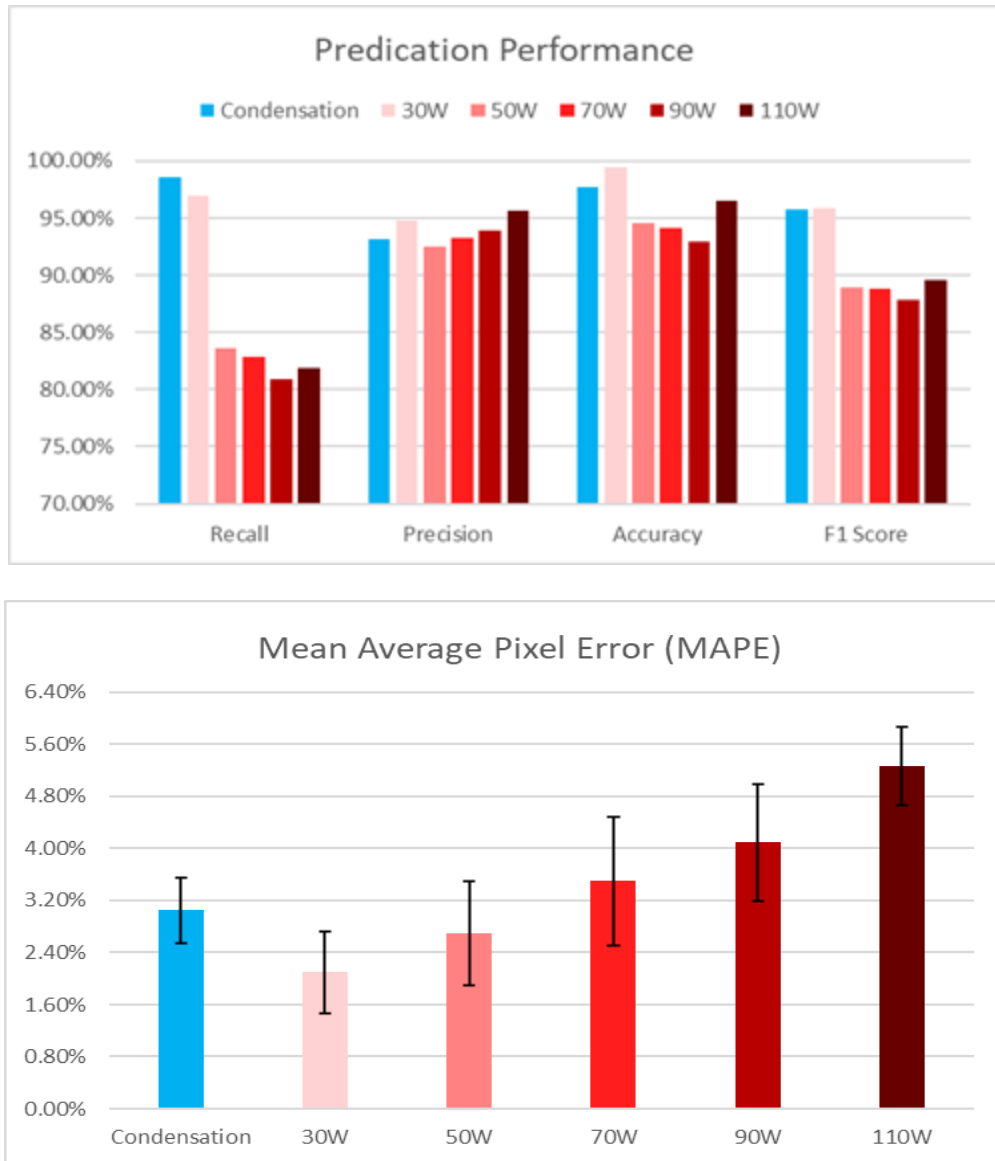
Figure 10. Mask R-CNN prediction performance is shown for condensation and various boiling datasets.
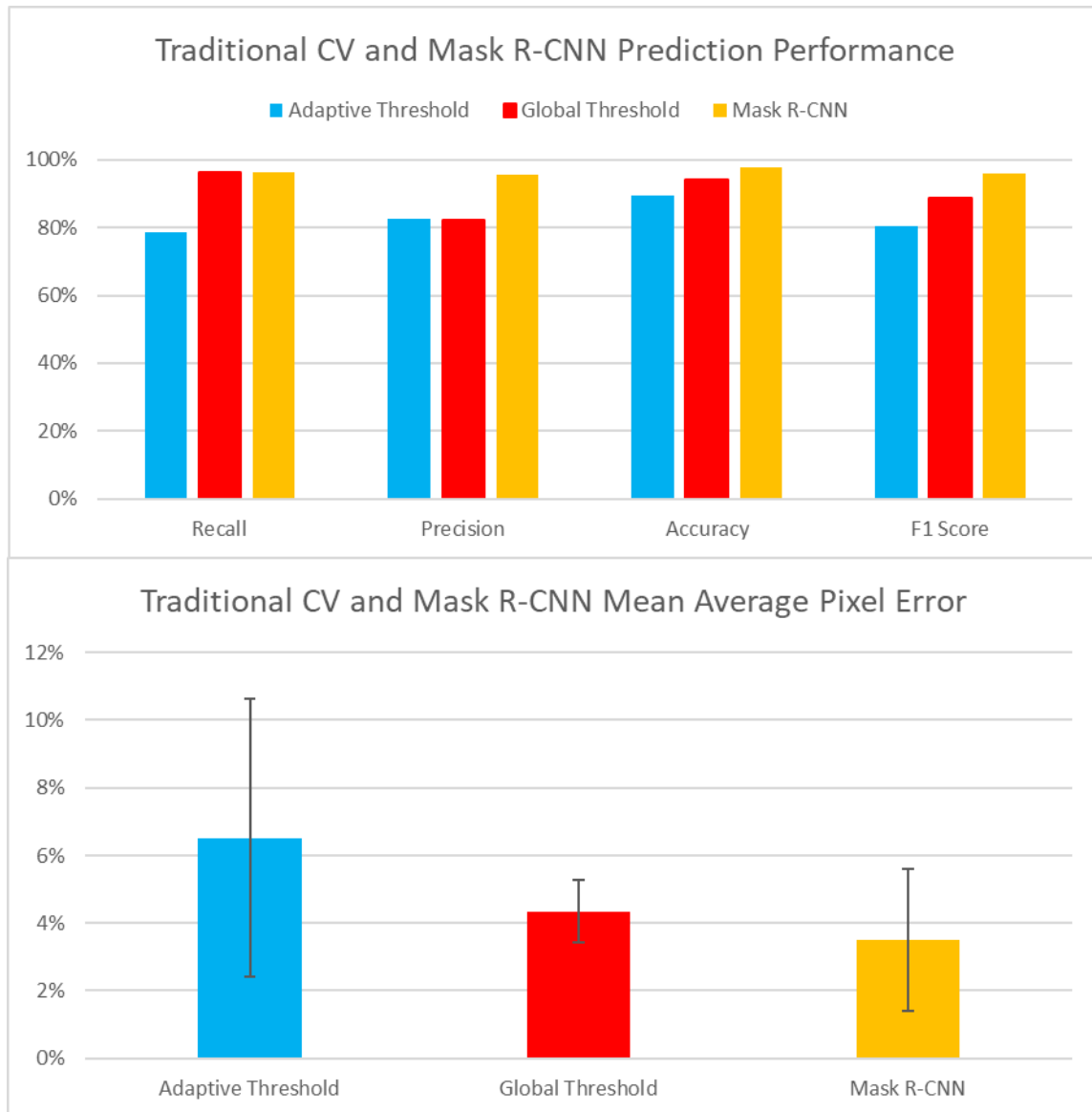
Figure 11. Object detection performance metrics shown for adaptive threshold, global threshold, and Mask R-CNN.

3.4 Inherent Issues with Phase Change Analysis

The surfaces within phase change experiments produce an overwhelming amount of nucleation events. These nucleation events are directly related to the amount of heat dissipated from the system. Thus, accurate quantification of nucleation dynamics requires consistent and precise multiple object tracking. Multiple object tracking relies on accurate

detections generated by the object detector to produce precise object tracks. Incorrect detections created by the object detector will yield inaccurate object tracks. However, tracking based errors can also affect the accuracy of the results. Tracking based errors originate within the tracking algorithm independent of the detection accuracy. Tracking errors are denoted by incorrect, inconsistent object ID assignment across multiple frames.

Detection and tracking based errors ultimately lead to invalid object trajectories, where nucleation statistics are distorted resulting in erroneous heat transfer quantification. Since heat flux mappings are highly dependent on individual bubble growth rate, a small fluctuation in nucleation statistics will scale to a large fluctuation in heat flux. The figure below shows an example of inaccurate object tracking.

Figure 12. Example of inaccurate tracking of nucleating bubbles within a pool boiling experiment.

This inherent prediction fluctuation can be alleviated by implementing moving average analysis. Moving average analysis will "flatten" the fluctuating heat flux mappings by
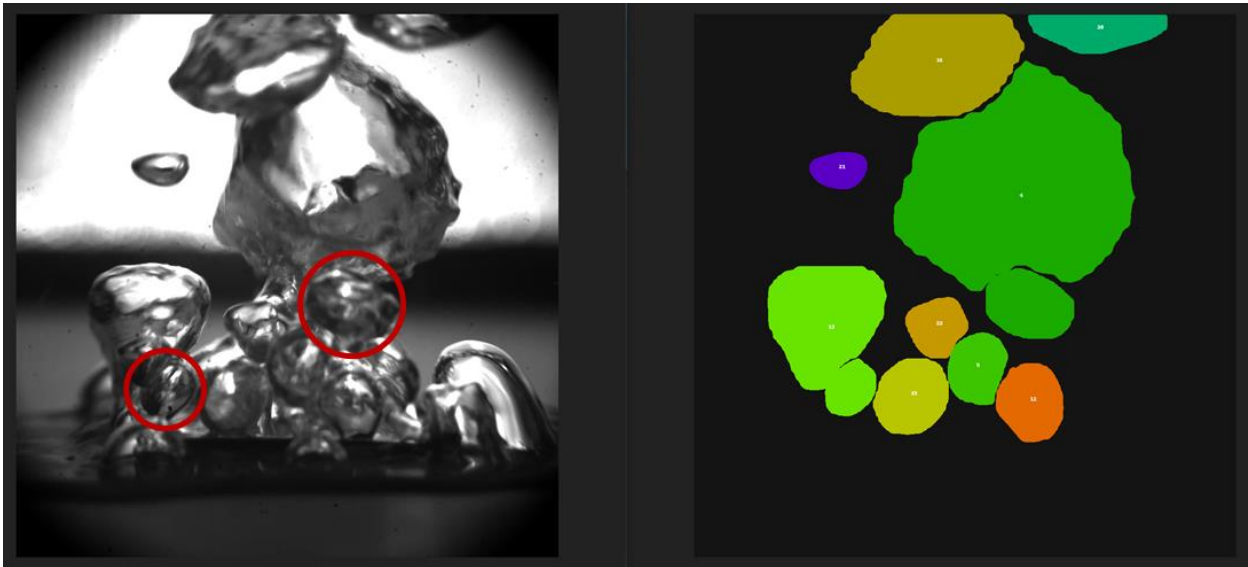
calculating the average of different subsets within the dataset.[40] The tracking algorithm requires fine-tuning of hyperparameters to mitigate any tracking errors.

3.4.1 Tracking Complex Dynamics

An innate feature of MASK R-CNN is that it is difficult to track small, similar objects that overlap each other.[41] Occlusion induced errors lead to improper object detection which result in invalid object ID assignment and inaccurate spatiotemporal data. This detection-based error leads to the tracking module producing inaccurate object trajectories. This error is predominately caused by bubbles in the front of the boiling surface covering bubbles in the rear. To determine how much occlusion induced error is present, separate annotations are created to account for occlusion events. The error within an image must solely be due to occlusion to be annotated for occlusion induced error. The annotation should only include the bubble that was missed due to being covered by another bubble. An example of an occlusion specific annotation is shown in Figure 13a. The plot below shows the occlusion-induced error for each heat flux. For phase change experiments, the maximum occlusion induced error is 4.6%. This error is relatively small compared to conventional measuring techniques and can be accounted for in calculations.[42] Occlusion induced errors could not be mitigated due to the reduced dimensionality of two-dimensional images describing the intricate nucleation dynamics of a three-dimensional system. Other studies with similar difficulties regarding occlusion induced error show that the implementation of multiple cameras can solve the problem; however, this is a more costly and complex experimental setup.[43]
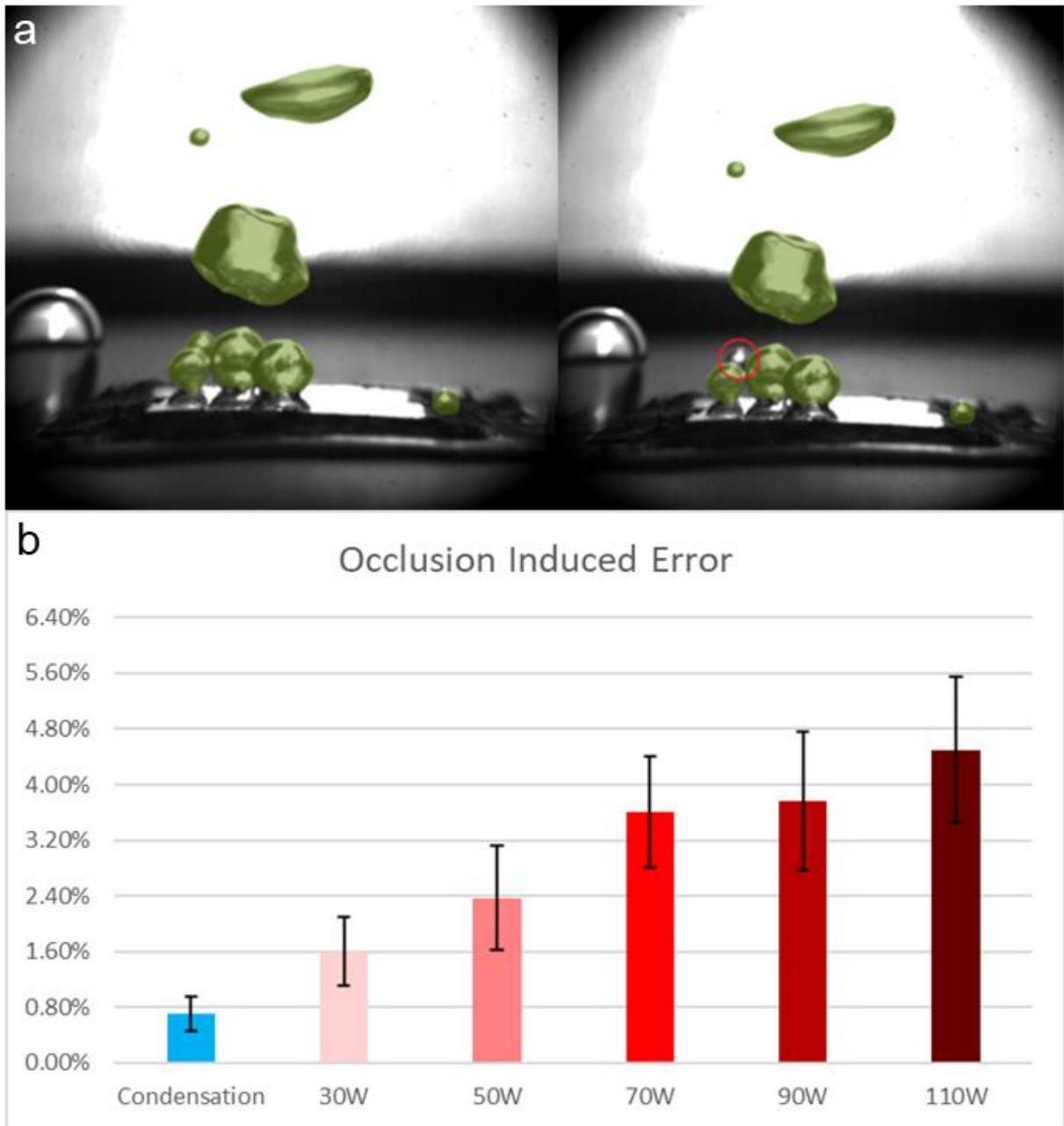
Figure 13. The red circle in the right image indicates an occlusion error, where the bubble is partially covered by other bubbles. The left-hand image shows an example of an occlusion specific annotation (a). Plot showing occlusion induced error for condensation and various boiling datasets (b).
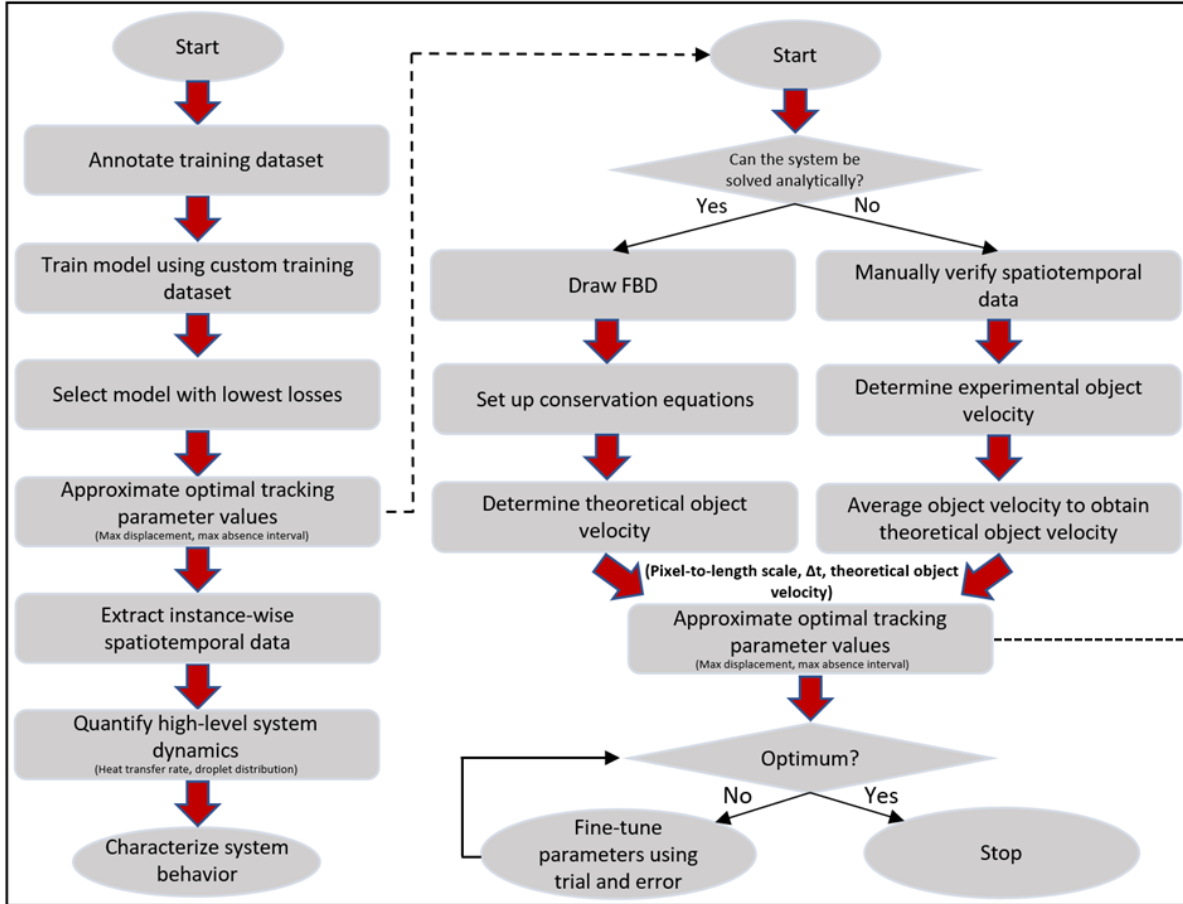
3.4.2 Object Tracking Parameter Optimization

The object tracker connects detection hypotheses throughout a series of frames to form object trajectories. The trajectories are calculated using object features from consecutive frames. To link the trajectories across each frame, the algorithm compares all possible trajectories and determines which is the most probable position for each object. The tracking parameters that must be fine-tuned for optimal performance include the distance cut-off factor (δ) and the maximum absence interval (ɣ).

The tracking module utilizes a distance cut-off factor (max displacement), the furthest distance an object can travel before being considered a new object. The optimal distance cut-off factor varies depending on system dynamics and data capture rate. In this paper, we have developed a procedure to determine the optimal distance cut-off factor for any dataset. First, determine the theoretical object velocity (φ) using analytical methods including conservation of mass, momentum, and energy. A valid model of the system will accurately approximate the theoretical object velocity. The equation below is used to determine the optimal distance cut-off, where $(t_j - t_{j-1})$ is defined as the time difference between trajectories.

$$\delta = \Phi * (t_j - t_{j-1})$$

If the system dynamics cannot be described using analytical solutions, the theoretical object velocity can be approximated using manually verified spatiotemporal results. To approximate theoretical object velocity, we calculate the average velocity across all detected objects. Using the average object velocity and the time between frames, the optimal distance cut-off factor can be calculated.

Figure 14. A diagram demonstrating the steps to train the framework and determine optimal tracking parameters.

In the case that an object is not detected in the sequential frame, the tracker retains an array of these "missing" objects for a certain number of frames. The number of frames is referred to as the maximum absence interval. For example, a maximum absence interval of two indicates that an object can vanish for two frames, reappear, and be considered the same object. The figure below shows examples of errors associated with max absence interval and distance cut-off factor. The optimal maximum absence interval can be determined by investigating which γ value yields the most accurate spatiotemporal results. With our approach of optimizing γ and δ, the tracking module will produce consistent and reliable results. Tracking performance with varying tracking hyperparameters among several heat flux steps shows that the value of the hyperparameters directly affects tracking performance. The predefined parameters cannot account for low heat flux and high heat flux motion at the same time. Thus, tracking parameters were adjusted for each heat flux step to optimize tracking results. For lower heat flux datasets, the optimal max displacement was found to be around 100 pixels. The middle heat flux datasets (50 - 70W) had an optimal max displacement of around 150 pixels. The high heat flux datasets (90 - 100W) achieved optimal tracking with a max displacement of 200 pixels.
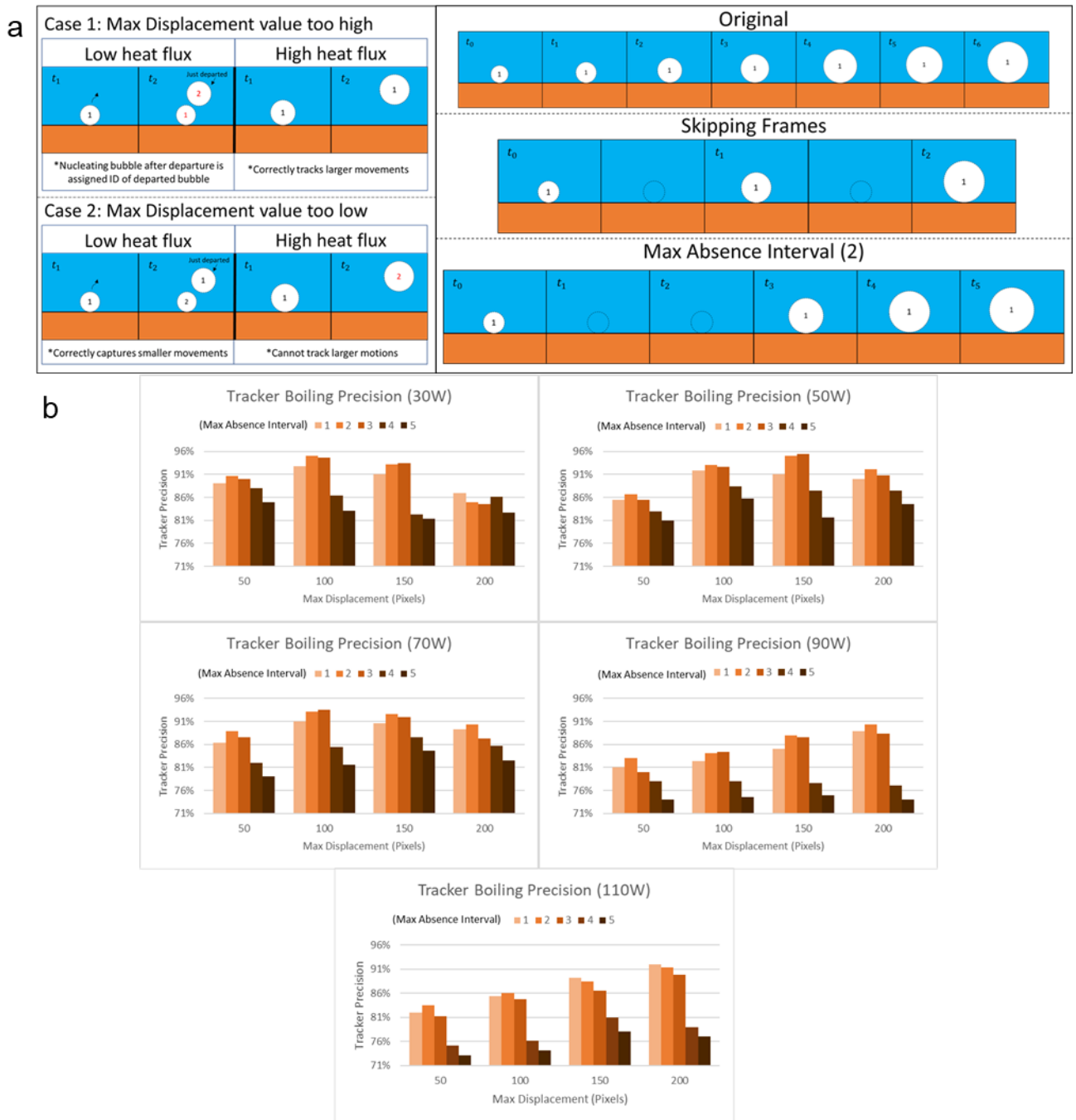
Figure 15. Tracking issues associated with max displacement and max absence interval tracking parameters are shown in (a). Tracking performance with varying tracking hyperparameters for various heat flux steps is shown (b).

Chapter 4

This chapter discusses future opportunities to study phase change processes as well as potential challenges when using artificial intelligence-based frameworks. Future research directions are also reviewed.

Conclusion

In conclusion, the proposed artificial intelligence-based framework enables thermofluidic engineers to customize the model to perform different tasks for various experimental setups (i.e., surface features, working fluid, experiment configuration). This framework has the potential to discover unknown relationships within complex phase change systems by automatically extracting object-specific spatiotemporal features of nucleation events. Nonetheless, the governing physics behind phase change is still largely theoretical due to weak correlations between nucleation statistics and heat transfer. This is owing to the difficulty of extracting nucleation statistics from surfaces with large bubble densities. However, the proposed framework enables the collection of nucleation statistics to study various phase change systems. For example, surface-dependent heat transfer models can be generated using the extracted data from various surfaces (i.e., bare copper, sintered copper). Additionally, the relationship between bubble departure dynamics and heat transfer performance within pool boiling can be further investigated. Moreover, researchers can explore the effects of droplet removal via coalescence-induced events (i.e., droplet jumping) occurring within condensation experiments.

However, accurate object tracking at high spatiotemporal resolutions remains a challenge due to detection-based and tracking based errors. Precise annotations quantify the

magnitude of detection-based errors while experimental setups consisting of multiple cameras reduce these errors. The proposed tracking parameter optimization process generates ideal tracking parameters to minimize tracking-based errors.

One primary concern in phase change thermal management systems is the lifetime expectancy of the phase change surface. The proposed model has potential to identify when surface deterioration begins to occur by autonomously observing changes in nucleation events (e.g., bubble growth, departure frequency). Excessive void fraction within flow boiling systems also causes sudden and premature failure within thermal management systems. Current studies are investigating the performance of flow boiling prediction models, where void fraction is calculated using binarized images.

AI vision-based frameworks are advantageous due to minimal computational costs and experimental setup required. For example, the model is capable of instantly extracting bubble features over different experimental setups due to non-invasive measurement techniques requiring only a high-speed camera and a computer with a trained model. The model also has potential to significantly reduce computation time for thermofluidic engineers by eliminating the time-consuming task of manually identifying each nucleation event over a large dataset.

Furthermore, the prediction performance script developed has the potential for determining the performance of any vision-based object detection framework. For instance, the performance of autonomous vehicle sensors exposed to extreme conditions can be determined using the prediction performance script. This allows researchers to determine the effect of various factors on the performance of vision-based object detection frameworks.

The development of a non-invasive autonomous model enables researchers to quantify the heat transfer performance of newly engineered surfaces at an astonishing rate. As thermofluidic engineers progress in the urgent search for more efficient phase change surfaces, heat transfer models will continue to reveal the underlying physics governing phase change processes. As future work, the relationship between void fraction and heat transfer performance within flow boiling will be investigated.

REFERENCES

1. Rupp, K. In *48 years of microprocessor trend data*, GitHub, **2020**.

2. Ebadian, M. A.; Lin, C. X. A review of high-heat-flux heat removal technologies. *Journal of Heat Transfer* **2011**, *133*.

3. Ganatra, Y.; Ruiz, J.; Howarter, J. A.; Marconnet, A. Experimental investigation of phase change materials for thermal management of handheld devices. *International Journal of Thermal Sciences* **2018**, *129*, 358–364.

4. Kozyrakis, C.; Kansal, A.; Sankar, S.; Vaid, K. Server engineering insights for large-scale online services. *IEEE Micro* **2010**, *30*, 8–19.

5. Baig, T.; Rehman, Z.; Tariq, H. A.; Manzoor, S.; Ali, M.; Wadood, A.; Rajski, K.; Park, H. Thermal performance investigation of slotted fin minichannel heat sink for microprocessor cooling. *Energies* **2021**, *14*, 6347.

6. Rau, M. J. Phase-change thermal management solutions for advanced electronics. *2018 IEEE CPMT Symposium Japan (ICSJ)* **2018**.

7. Tsuchiya, H.; Manabe, K.; Gaudelet, T.; Moriya, T.; Suwabe, K.; Tenjimbayashi, M.; Kyong, K.-H.; Gillot, F.; Shiratori, S. Improvement of heat transfer by promoting dropwise condensation using electrospun polytetrafluoroethylene thin films. *New Journal of Chemistry* **2017**, *41*, 982–991.

8. Balaji, C.; Srinivasan, B.; Gedupudi, S. Boiling and condensation. *Heat Transfer Engineering* **2021**, 351–396.

9. Konishi, C.; Mudawar, I. Review of flow boiling and critical heat flux in microgravity. *International Journal of Heat and Mass Transfer* **2015**, *80*, 469–493.

10. Devahdhanush, V. S.; Mudawar, I. Review of Critical Heat Flux (CHF) in jet impingement boiling. *International Journal of Heat and Mass Transfer* **2021**, *169*, 120893.

11. Mudawar, I. Recent advances in high-flux, two-phase thermal management. *Journal of Thermal Science and Engineering Applications* **2013**, *5*.

12. Benther, J. D.; Pelaez-Restrepo, J. D.; Stanley, C.; Rosengarten, G. Heat transfer during multiple droplet impingement and spray cooling: Review and prospects for enhanced surfaces. *International Journal of Heat and Mass Transfer* **2021**, *178*, 121587.

13. Chi-Yeh, H.; Griffith, P. The mechanism of heat transfer in nucleate pool boiling—part I. *International Journal of Heat and Mass Transfer* **1965**, *8*, 887–904.

14. Devahdhanush, V. S.; Lei, Y.; Chen, Z.; Mudawar, I. Assessing advantages and disadvantages of macro- and micro-channel flow boiling for high-heat-flux thermal management using computational and theoretical/empirical methods. *International Journal of Heat and Mass Transfer* **2021**, *169*, 120787.

15. Imura, H.; Sasaguchi, K.; Kozai, H.; Numata, S. Critical heat flux in a closed two-phase thermosyphon. *International Journal of Heat and Mass Transfer* **1983**, *26*, 1181–1188.

16. Sato, Y.; Niceno, B. Pool boiling simulation using an interface tracking method: From nucleate boiling to film boiling regime through critical heat flux. *International Journal of Heat and Mass Transfer* **2018**, *125*, 876–890.

17. Ded, J. S.; Lienhard, J. H. The peak pool boiling heat flux from a sphere. *AIChE Journal* **1972**, *18*, 337–342.

18. Kim, H.; Park, Y.; Buongiorno, J. Measurement of wetted area fraction in subcooled pool boiling of water using infrared thermography. *Nuclear Engineering and Design* **2013**, *264*, 103–110.

19. Jingliang, B.; Xipeng, L.; Christopher, D. M. Effects of bubble coalescence dynamics on heat flux distributions under bubbles. *AIChE Journal* **2012**, *59*, 1735–1745.

20. Lee, D.; Lim, J.-S.; Lee, N.; Cho, H. H. Enhanced Thermal Uniformity and stability in pool boiling heat transfer using ultrasonic actuation. *International Communications in Heat and Mass Transfer* **2019**, *106*, 22–30.

21. Barbosa, J. R.; Govan, A. H.; Hewitt, G. F. Visualisation and modelling studies of churn flow in a vertical pipe. *International Journal of Multiphase Flow* **2001**, *27*, 2105–2127.

22. Waltrich, P. J.; Falcone, G.; Barbosa, J. R. Axial development of annular, churn and slug flows in a long vertical tube. *International Journal of Multiphase Flow* **2013**, *57*, 38–48.

23. Oktar, Y.; Ulucan, O.; Karakaya, D.; Ersoy, E. O.; Turkan, M. Binocular vision based Convolutional Networks. *2020 28th Signal Processing and Communications Applications Conference (SIU)* **2020**.

24. Aladem, M.; Rawashdeh, S. A. A single-stream segmentation and depth prediction CNN for autonomous driving. *IEEE Intelligent Systems* **2021**, *36*, 79–85.

25. Favorskaya, M.; Pakhirka, A. Animal species recognition in the wildlife based on muzzle and shape features using joint CNN. *Procedia Computer Science* **2019**, *159*, 933–942.

26. Xie, B.; Zhang, H. K.; Xue, J. Deep Convolutional Neural Network for mapping smallholder agriculture using High Spatial Resolution Satellite Image. *Sensors* **2019**, *19*, 2398.

27. He, K., Gkioxari, G., Dollár, P. & Girshick, R. Mask R-CNN. *In Proceedings of the IEEE international conference on computer vision* **2017**, 2961–2969.

28. Hobold, G. M.; da Silva, A. K. Machine learning classification of boiling regimes with low speed, direct and indirect visualization. *International Journal of Heat and Mass Transfer* **2018**, *125*, 1296–1309.

29. Hobold, G. M.; da Silva, A. K. Visualization-based nucleate boiling heat flux quantification using machine learning. *International Journal of Heat and Mass Transfer* **2019**, *134*, 511–520.

30. Suh, Y.; Lee, J.; Simadiris, P.; Yan, X.; Sett, S.; Li, L.; Rabbi, K. F.; Miljkovic, N.; Won, Y. A deep learning perspective on dropwise condensation. *Advanced Science* **2021**, 2101794.

31. Tsai, H.-F.; Gajda, J.; Sloan, T. F. W.; Rares, A.; Shen, A. Q. USIIGACI: Instance-aware cell tracking in stain-free phase contrast microscopy enabled by machine learning. *SoftwareX* **2019**, *9*, 230–237.

32. Son, G.; Dhir, V. K.; Ramanujapu, N. Dynamics and heat transfer associated with a single bubble during nucleate boiling on a horizontal surface. *Journal of Heat Transfer* **1999**, *121*, 623–631.

33. Guan, Q.; Wang, Y.; Ping, B.; Li, D.; Du, J.; Qin, Y.; Lu, H.; Wan, X.; Xiang, J. Deep convolutional neural network VGG-16 model for differential diagnosing of papillary thyroid carcinomas in cytological images: A pilot study. *Journal of Cancer* **2019**, *10*, 4876–4882.

34. Devnani, G.; Jaiswal, A.; John, R.; Chaurasia, R.; Tirpude, N. Performance evaluation of fine-tuned faster R-CNN on specific MS coco objects. *International Journal of Electrical and Computer Engineering (IJECE)* **2019**, *9*, 2548.

35. Suh, Y.; Bostanabad, R.; Won, Y. Deep learning predicts boiling heat transfer. *Scientific Reports* **2021**, *11*.

36. Kim, M.-K.; Cha, H.; Birbarah, P.; Chavan, S.; Zhong, C.; Xu, Y.; Miljkovic, N. Enhanced jumping-droplet departure. *Langmuir* **2015**, *31*, 13452–13466.

37. Mikolajczyk, A.; Grochowski, M. Data augmentation for improving deep learning in image classification problem. *2018 International Interdisciplinary PhD Workshop (IIPhDW)* 2018.

38. S. Visa, B. Ramsay, A. L. Ralescu, E. Van Der Knaap: Confusion Matrix-based Feature Selection. *MAICS* 2011, *710*, 120-127.

39. D. M. Powers: Evaluation: from precision, recall and F-measure to ROC, informedness, markedness and correlation. *arXiv preprint arXiv:2010.16061*, (2020).

40. Durbin, J. Efficient estimation of parameters in moving-average models. *Biometrika* 1959, *46*, 306.

41. Huang, E.; Mao, A.; Ceballos, M. C.; Parsons, T. D.; Liu, K. Capacity limit of deep learning methods on scenarios of pigs in farrowing pen under occlusion. *2021 ASABE Annual International Virtual Meeting,* 2021.

42. Liu, Zhi-Yong, Estimation of heat of vaporization of pure liquid at its normal boiling temperature. *Chemical Engineering Communications* 2001, *184*, 221–228.

43. Baque, P.; Fleuret, F.; Fua, P. Deep occlusion reasoning for multi-camera multi-target detection. *2017 IEEE International Conference on Computer Vision (ICCV)* 2017.